Energy 177 (2019) 247–261

Contents lists available at ScienceDirect

Energy

journal homepage: www.elsevier.com/locate/energy

Bi-objective optimal design of plug-in hybrid electric propulsion system for ships

Zhu Jianyun, Chen Li*, Xia Lijuan, Wang Bin

State Key Laboratory of Ocean Engineering of Shanghai Jiao Tong University, Key Laboratory of Marine Intelligent Equipment and System of Ministry of Education, Shanghai Jiao Tong University, PR China

ARTICLE INFO

Article history:
Received 21 October 2018
Received in revised form
6 March 2019
Accepted 14 April 2019
Available online 17 April 2019

Keywords:
Hybrid electric propulsion system
Bi-objective optimization
Fuel consumption
GHG emissions
NSGA-II
Sensitivity analysis

ABSTRACT

Growing concerns about reducing fuel consumption and global greenhouse gas (GHG) emissions have forced the shipping industry to accelerate the development of plug-in hybrid electric propulsion systems (HEPSs). However, the design optimization of plug-in HEPSs with the single objective of saving fuel may result in increased GHG emissions. This study proposes a bi-objective optimization by considering not only fuel consumption but also GHG emissions. The NSGA-II method is developed to explore the Pareto optimal solution set. A real-time hardware-in-the-loop experimental platform is built to validate the effectiveness of the optimization. The experimental results show that the optimal design selected from the Pareto solution set of the bi-objective optimization is closer to the ideal point than the optimal designs via the single-objective optimization pursuing either minimum fuel consumption or minimum GHG emissions. Further, sensitivity analysis is conducted. It is found that three variables (motor rotor diameter, motor rotor length, and gear ratio) are of local optimum at the Pareto front; and two (number of battery modules and lower bound of the battery state of charge) are of strong sensitivity regarding the contradiction between fuel consumption and GHG emissions.

1. Introduction

Regarding environmental protection, an increasing number of stringent regulations on fuel consumption and emissions are being enacted in the shipping industry, such as the energy efficiency design index (EEDI) [1] and International Convention for the Prevention of Pollution from Ships (MARPOL convention) [2]. Hybrid electric propulsion systems (HEPSs) are considered as one potential solution because diesel engines can work within the high efficiency region under various working conditions with the aid of electric machines [3–5]. Moreover, through the use of shore power that is charged into large capacity batteries, plug-in HEPSs can reduce further fuel consumption and extend the zero-emission range when operated in pure electric mode. Recently, the design of plug-in HEPSs has attracted increasing interest from both industry and academia [6,7].

In general, larger battery capacity allows more electricity from the shore power plant to be used, which means less fuel consumption and less emission on the voyage of plug-in HEPSs. However, the lifecycle greenhouse gas (GHG) emissions from the electricity production by coal is higher than that by fossil fuels and other renewable sources because coal is more carbon-intensive [8]. In countries rich in coal, such as China and India, electricity is mainly produced by coal [9]. Thus, the overall GHG emissions of the plug-in HEPS might increase due to the over usage of the shore power. Therefore, it is necessary to optimize the design of the plug-in HEPS considering not only fuel consumption but also GHG emissions.

In most previous studies, design optimization was performed only with the goal of fuel saving while GHG emissions were not considered in the objective function. The design of a serial HEPS was optimized for a medium-size (14 m) boat [10]. The fuel consumption of the optimal design is 61.8 L/100 km, compared to 92.6 L/100 km of the conventional design. Two optimal designs, that can reduce energy consumption by 8%, on average, across four typical scenarios, were examined for a hybrid steam turbine/electric motor propulsion system [11]. With the aim to be fuel-saving and weight-saving, the HEPS size was optimized for a motoryacht [12]. However, fuel saving does not necessarily mean low GHG emissions. Specifically, GHG emission reduction, even zero

* Corresponding author. Mulan Building B629, Shanghai Jiao Tong University, 800 Dong Chuan Rd., Shanghai, 200240, PR China.
E-mail address: li.h.chen@sjtu.edu.cn (C. Li).

https://doi.org/10.1016/j.energy.2019.04.079
0360-5442/

emission, is a major requirement for the usage of HEPSs in some key environmentally protected areas. Thereafter, it is important to examine a bi-objective optimization design to achieve a compromise regarding fuel consumption and GHG emissions.

Bi-objective optimization can obtain better designs in terms of comprehensive performance when compared with single-objective optimization. For example, a plug-in fuel cell hybrid bus reduces fuel consumption by 12.86% while lowering GHG emissions by 9.36% [13]. An optimization considering HC/CO/NO_x emissions and fuel consumption was applied to a hybrid electric vehicle [14]. However, bi-objective optimization considering fuel consumption and GHG emissions simultaneously has not been explored for diesel-electric hybrid vehicles and HEPS ships. In addition, there are significant differences between the hybrid vehicles and HEPS ships. First, long range and durable endurance is essential for HEPS ships, whereas hybrid vehicles can be refilled, recharged, or repaired conveniently. Second, a much larger amount of non-propulsive power is generally required by HEPS ships to drive working devices, such as crane and water treatment, while the auxiliary power requirement of hybrid vehicles is relatively low. Third, HEPS ships typically use multiple generator sets or even multiple types of prime movers that are connected to a common power bus and are independently controlled. In contrast, hybrid vehicles typically use a set of power devices. Fourth, unlike hybrid vehicles that are likely to stop-and-go frequently, HEPS ships typically keeps sailing in one mode for a long time with a stable power requirement. Finally, it is inefficient to apply regenerative braking technology due to the lack of direct adhesion between the propeller and water [15].

Several optimization algorithms have been recently developed for bi-objective and multi-objective problems in various applications. The weighting factor method was examined to solve an active distribution networks planning problem in order to minimize the total operational cost and total energy loss [16]. The selection of weighting factors is challenging because different combinations of weighting factors results in optimal designs which achieve different performance. Instead of using weighting factors, the Pareto optimal solution set provides an effective method to deal with multi-objective optimization problems. For example, a multi-objective ant colony optimization (MOACO) algorithm was designed to solve a path-finding problem for a military unit aiming to pursuing maximum speed and safety [17]. However, the MOACO always involves a long period to reach convergence and tends to be confined to a local optimum solution. A non-dominated sorting genetic algorithm II (NSGA-II), which is an evolutionary-based global optimization, has been applied to the absorption heat pump [18], Stirling heat pump [19], refrigerator [20], irreversible regenerative closed Brayton cycle [21], multi-step solar-driven Brayton plant [22], etc. The NSGA-II was compared with another multi-objective particle swarm optimization algorithm (MOPSO) to solve a multi-objective multi-route flexible flow line problem [23]. The results indicated that the NSGA-II performs better than MOPSO in terms of space and quality criteria, though the NSGA-II provides fewer Pareto solutions. In addition, the NSGA-II was compared with a dominance based multi-objective simulated annealing algorithm (DBMOSA) in the optimization of network design. The results showed that the NSGA-II outperforms the DBMOSA in global searching ability [24]. Therefore, in the present study, the NSGA-II is chosen to explore the design space.

Considering fuel consumption and GHG emissions, the present study proposes a bi-objective optimization methodology to determine the size of the major components of plug-in HEPSs, including the diesel engines, motors, battery modules, and gearboxes. The proposed methodology is applied to a 120-ton tug ship equipped with a set of plug-in HEPS. The Pareto solution sets calculated from the NSGA-II are compared with the optimal solution from a single objective algorithm considering fuel consumption and GHG emissions. The performance tests are performed on a hardware-in-the-loop (HIL) platform. Furthermore, sensitivity analysis is performed in order to understand and provide insight into the results from optimization.

The present study is organized as follows. Section 2 builds the mathematical models of the plug-in HEPS. Section 3 describes the energy management strategy. Section 4 presents the optimization algorithm. Section 5 provides the results and discussion, and section 6 draws conclusions.

2. Mathematical modeling

The configuration of a plug-in HEPS is compared with that of a conventional propulsion system, as shown in Fig. 1. In the conventional propulsion system, four diesel engines are used, two drive two propellers, and two drive two generators. The two propellers are identical and symmetrically arranged along the longitudinal axis of the ship. The two generators are identical.

However, in the plug-in HEPS, only two diesel engines are used. They drive two identical generators and produce electricity distributed by the power bus. Other than the two generators, the power bus distributes the electricity from two additional sources, i.e., the battery and the shore power station. Two motors use the electricity and each drive one of the two propellers. The battery can store the electricity from the shore power and generators, and help supply the power required by the propellers, hotel load, and service load. Thus, the diesel engines are not directly connected to the propellers, so they can work within high efficiency range in terms of rotary velocity and output torque regardless of changes in power demand. Additionally, more electricity from the shore power

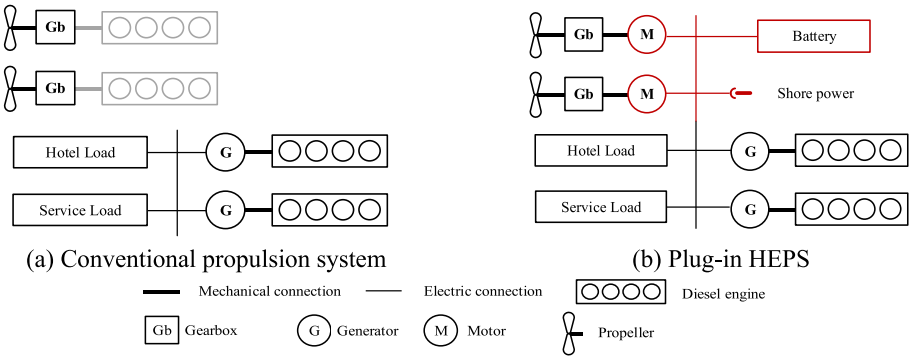

Fig. 1. Diagram of propulsion systems.

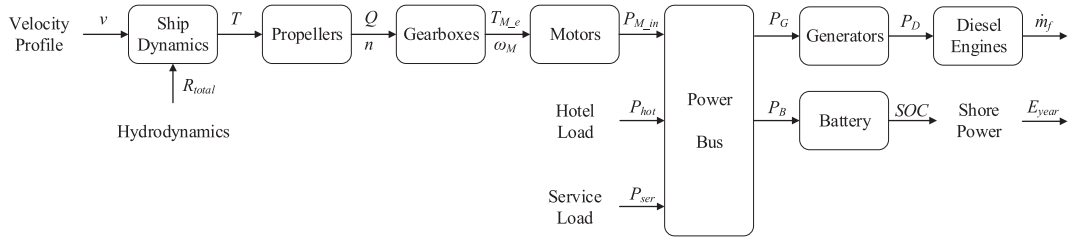

Fig. 2. Information flow of the mathematical models.

station allows longer range of zero-emission during the voyage.

To facilitate the optimization algorithm, the plug-in HEPS is modeled using the inverse simulation method [25]. For a predefined velocity profile, the thrust T of the propeller can be calculated from the models of ship dynamics and hydrodynamics as shown in Fig. 2. Following that, the physical quantities (rotary velocity, torque, power, etc.) of the propellers, motors, generators, and diesel engines can be calculated by using the mathematical models. The models illustrated in Fig. 2 are detailed in the following paragraphs.

2.1. Ship dynamics

The longitudinal dynamics of the ship is given by Refs. [26,27]:

$$m\frac{\mathrm{d}v}{\mathrm{d}t} = n_p T(1-t_1) - R_{total}. \tag{1}$$

where m is the mass of the ship, v is the velocity of the ship, n_p is the number of the propellers, T is the effective thrust of one propeller, t_1 is the thrust deduction coefficient, and R_{total} is the total resistance calculated from hydrodynamics including frictional resistance R_F, wave-making resistanceR_W, air resistance R_{Air} [27,28] as below.

$$R_{total} = R_F + R_W + R_{Air}. \tag{2}$$

$$R_F = \frac{1}{2}C_F\rho v^2 S. \tag{3}$$

$$R_W = \frac{1}{2}C_W\rho v^2 S. \tag{4}$$

$$R_{Air} = \frac{1}{2}C_{Air}\rho v^2 A_T. \tag{5}$$

where, ρ is the sea-water density, S is the wet-surface area of hull, C_F is the frictional resistance coefficient, C_W is the wave-making resistance coefficient, C_{air} is the air resistance coefficient, A_T is the advance facing area in the air.

2.2. Propellers

The two propellers are identical. For each propeller, the effective thrust T and the effective torque Q are given by Refs. [27,28]:

$$T = K_T n^2 D^4 \rho. \tag{6}$$

$$Q = n^2 D^5 \rho K_Q. \tag{7}$$

$$K_T = f_T(J_A, pitch/D, A_e/A_o, Z, R_n). \tag{8}$$

$$K_Q = f_Q(J_A, pitch/D, A_e/A_o, Z, R_n). \tag{9}$$

where K_T is the thrust coefficient, K_Q is the torque coefficients, n is the angular speed whose units is rpm (revolution per minute), D is the diameter, A_e and A_0 are the expanded blade area and swept area of the propellers, respectively. The coefficients K_T and K_Q are the functions of the advance coefficient J_A, pitch ratio$pitch/D$, expanded blade—area ratio A_e/A_0, number of propeller blades Z, and Reynolds number R_n [29]. The definitions of J_A and R_n are given as below.

$$J_A = \frac{v}{nD}. \tag{10}$$

$$R_n = \frac{1}{v}vD. \tag{11}$$

where v is the kinematic viscosity.

2.3. Gearboxes

Each propeller requires a gearbox to connect the driving motor. Therefore, there are two identical gearboxes. Each gearbox is modeled as below.

$$\omega_M = \frac{2\pi i}{60}n. \tag{12}$$

$$T_{M\_e} = \frac{1}{i\eta_{gear}}Q. \tag{13}$$

where ω_M is the angular velocity of the motor, T_{M_e} is the output torque of the motor, i is the gear ratio, and η_{gear} is the efficiency coefficient.

2.4. Motors

The two driving motors are identical. Each motor is described by a scalable model based on the Willans line method [30]. The Willans line method represents the relationship between the theoretically available energy and the output energy from energy converters. It is widely used to build scalable models for motors, gasoline engines, and diesel engines [31]. To establish the motor model, the available mean effective pressure p_{M_me} is defined as the mean force acting on the unit area of the rotor surface, and the break mean effective pressure p_{M_ma} expresses the maximum value of p_{M_me} if the efficiency of the motor is 100%.

$$p_{M\_me} = \frac{T_{M\_e}}{2V_{rotor}}. \tag{14}$$

$$p_{M\_ma} = \frac{P_{M\_in}}{2V_{rotor}\omega_M}. \tag{15}$$

$$V_{rotor} = \frac{1}{4}d_M^2 l_M. \tag{16}$$

where T_{M_e} and ω_M are the output torque and angular velocity of the motor, respectively. The volume of motor rotor V_{rotor} is calculated from the diameter d_M and length l_M of the motor rotor.

The relationship between the available mean effective pressure p_{M_me} and the break mean effective pressure p_{M_ma} can be expressed as [30]:

$$p_{M\_me} = -e_{M_2}\cdot p_{M\_ma}^2 + e_{M\_1}p_{M\_ma} - p_{M\_loss}. \tag{17}$$

$$\begin{aligned} p_{M\_loss} &= e_{M\_l2}\cdot v_r^2 + e_{M\_l0} \\ e_{M\_2} &= e_{M\_21}v_r + e_{M\_20} \\ e_{M\_1} &= e_{M\_12}v_r^2 + e_{M\_11}v_r + e_{M\_10} \\ v_r &= \frac{1}{2}d_M\omega_D \end{aligned}. \tag{18}$$

where,v_r is the average line speed of the motor rotor. The Willans line coefficients (e_{M_10}, e_{M_11}, e_{M_12}, e_{M_20}, e_{M_21}, $e_{M_l0}$and e_{M_l2}) are inherited by the new designed motor that belongs to the same class as the baseline motor.

Based on the efficiency map of a baseline motor, the Willans line coefficients for motor can be calculated by parameter identification from equation (17). Changing the diameter d_M and length l_M of the motor rotor, equation (17) can be used to represent the relationship between the available mean effective pressure p_{M_me} and the break mean effective pressure p_{M_ma} of a scaled motor, as well as the relationship between the input power P_{M_in} and operational conditions (T_{M_e} and ω_M).

2.5. Generators

The two generators are identical. The output power of each generator is denoted by P_G which is calculated by:

$$P_G = \eta_{gen}P_D. \tag{19}$$

$$P_{G\_rate} = \eta_{gen}P_{D\_rate}. \tag{20}$$

$$P_D = T_{D\_e}\cdot\omega_D. \tag{21}$$

where P_D is the output power of the diesel engine, η_{gen} is the efficiency of the generator, T_{D_e} is effective torque of the diesel engine, and ω_D is the angular velocity of the diesel engine. In general, the rated power P_{G_rate} of the generator is chosen to match the rated power P_{D_rate} of the corresponding diesel engine.

Given that the size of the diesel engine is discussed in detail in the following paragraphs, it is unnecessary to model and further investigate the size of the generator.

2.6. Diesel engines

A scalable model is established based on the Willans line method [30–33]. Firstly, the available mean effective pressure p_{D_ma} and break mean effective pressure p_{D_me} are defined as below.

$$p_{D\_me} = 4\pi\cdot\frac{T_{D\_e}}{V_D}. \tag{22}$$

$$p_{D\_ma} = L_{CV}\cdot\frac{4\pi}{V_D}\frac{\dot{m}_f}{\omega_D}. \tag{23}$$

in which, V_D is the diesel engine displacement, L_{CV} is the lower calorific value of the diesel fuel, and$\dot{m}_f$ is the mass flow of the diesel fuel. According to the Willans line method, the two pressures can be fitted by a polynomial as below [33].

$$p_{D\_me} = -e_{D_2}\cdot p_{D\_ma}^2 + e_{D\_1}p_{D\_ma} - p_{D\_loss}. \tag{24}$$

$$\begin{aligned} p_{D\_loss} &= e_{D\_l2}\cdot v_p^2 + e_{D\_l0} \\ e_{D\_2} &= e_{D\_21}v_p + e_{D\_20} \\ e_{D\_1} &= e_{D\_12}v_p^2 + e_{D\_11}v_p + e_{D\_10} \\ v_p &= \frac{S_D}{\pi}\omega_D \end{aligned}. \tag{25}$$

$$V_D = \frac{1}{4}S_D B_D^2. \tag{26}$$

where v_p is the average piston speed, S_D and B_D are the stroke and bore of the cylinder, respectivelye_{D_10}, e_{D_11}, e_{D_12}, e_{D_20}, e_{D_21}, e_{D_l0}, and e_{D_l2} are Willans line factors for diesel engine which are the same for a class of engine designs with different displacement V_D and stroke S_D.

Therefore, given the data of the available mean effective pressure p_{D_ma} and break mean effective pressure p_{D_me} of a baseline diesel engine, the Willans line factors can be obtained by parameter identification from (25). Thereafter, given the effective torque T_{D_e}, the displacement V_D and stroke S_D of a new diesel engine, the break mean effective pressure p_{D_me} can be calculated from (22). Following that, the available mean effective pressure p_{D_ma} can be calculated from (24). Finally, the mass flow $\dot{m}_f$ can be calculated from (23). e_{D_10}, e_{D_11}, e_{D_12}, e_{D_20}, e_{D_21}, e_{D_l0} ased on these calculations, the mass flow of a class of diesel engine designs can be obtained.

2.7. Battery

In this study, lithium-ion batteries are used due to their high energy density, prominent storage efficiency, and flat characteristic curve of voltage drop without memory effects [34]. In the battery system, several battery modules are connected in series. Each battery module consists of 40 identical battery cells which are parallelly connected. The number of battery modules, n_{ser}, should be designed. As applied to the analysis of other hybrid powertrains, the Rint model is used to describe the current I of the battery cell as below [35–38].

$$P_{bat} = \frac{P_B}{n_{ser}}. \tag{27}$$

$$I = \frac{V_{oc}}{2R_{bat}} - \sqrt{\left(\frac{V_{oc}}{2R_{bat}}\right)^2 - \frac{P_{bat}}{R_{bat}}}. \tag{28}$$

where P_B is the power of the battery system, V_{oc}, R_{bat}, and P_{bat} are open-circuit voltage, internal resistance, and terminal power of the battery cell, respectively.

Disregarding the imbalance of the battery cells, the stage of

charge of the battery module is the same as that of the battery cell. The battery state of charge (SOC) is determined from Ref. [35]:

$$\dot{SOC} = -\frac{I\eta_{colm}}{Q_{bat}}. \tag{29}$$

where η_{colm} is Coulombic efficiency, and Q_{bat} is the battery capacity.

3. Energy management strategy

The energy management strategy is used to coordinate the operation of the diesel engine, motor, and generator, also to coordinate the usage of electricity from the battery and the shore power plant, aiming to fulfill the power required by the propellers, hotel load, and service load of the plug-in HEPS. Considering low computational load and implementation convenience, a rule-based strategy is developed for the energy management of this study.

First of all, the battery should be charged to $SOC_0 = 90\%$ by the shore power plant before the ship starts the voyage. The energy management strategy prioritizes electricity from the shore because it generally reduces fuel consumption and is cleaner to local waters in comparison with energy from the generators produced by on-board diesel engines. The output power of the battery, denoted by P_B, is determined by the status of the battery and total load power P_{req}. Following that, the number of running generators, n_G (0, 1 or 2), can be selected. The constraints of the battery are represented by three parameters, i.e., b_{lower}, b_{upper} and P_{B_max}, which are the lower bound of SOC, upper bound of SOC, and maximum output power of the battery, respectively. In this study, the SOC bounds, b_{lower} and b_{upper}, are not set to be constant like those in literature [39,40]. Instead, they are tuned by the optimal design discussed in next section.

In terms of the direction of the electric energy flow, the operation of the plug-in HEPS can be classified into two modes, battery charging mode and battery discharging mode. The schematic diagram of the energy management strategy is given in Fig. 3, where P_{G_rate} denotes the rated power of the generator. In the battery charging mode, the generators supply all the load power and charge the battery at the same time, until the battery SOC is within an appropriate range. In battery discharging mode, the generators and battery supply the load power together.

The rules of the energy management strategy are described in the following paragraphs.

(1) The plug-in HEPS operates in battery charging mode in three cases: (a) the battery SOC is below b_{lower}; (b) the battery SOC is between b_{lower} and b_{upper}, and the output power of the generators is greater than the load power; and (c) the battery SOC reaches b_{upper}, and the output power of the generators is approximately equal to the load power (this is an extreme case that the generators work but the battery charge actually stops). In this mode, each generator operates in the high efficiency region. The number of running generators, n_G, is selected for a generator output power greater than the total load power, so the extra power can be used to charge the battery.

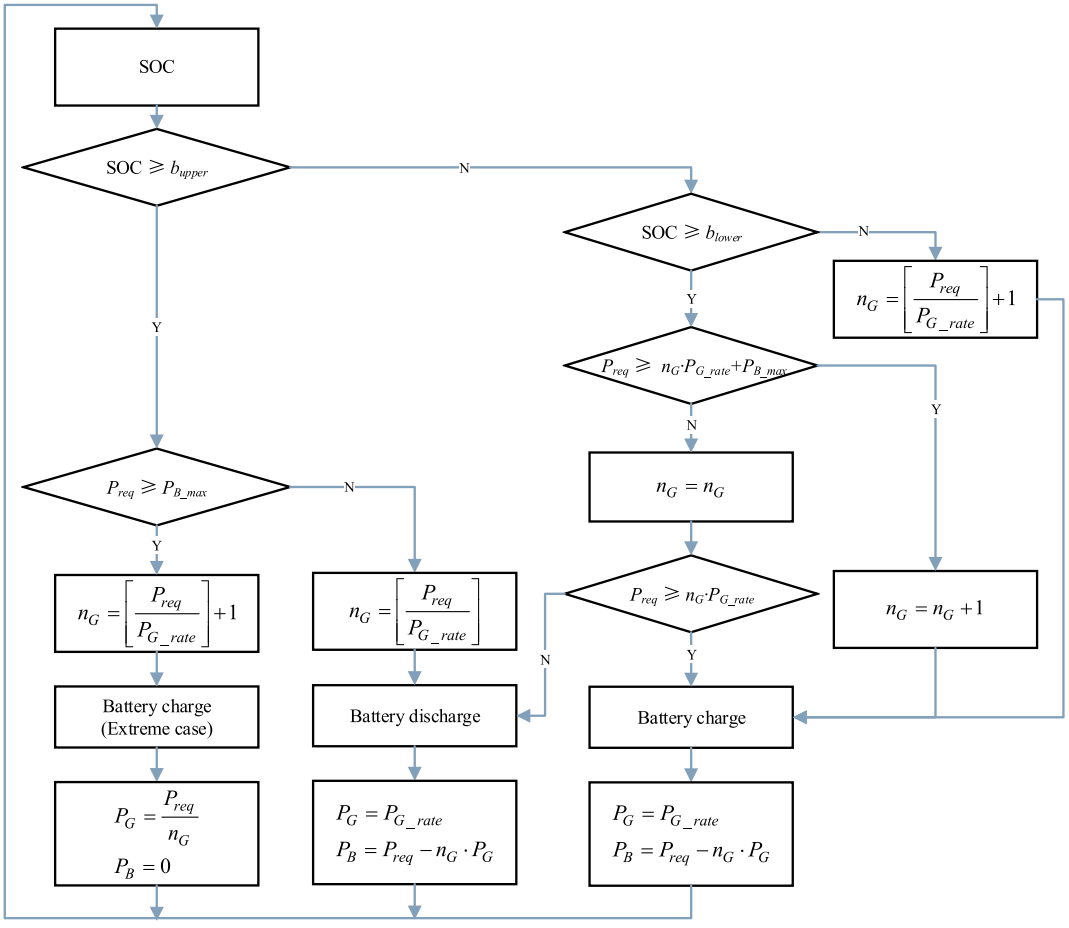

Fig. 3. Rule-based energy management strategy.

(2) The plug-in HEPS operates in battery discharging mode in two cases: (a) the battery SOC is higher than b_{upper}, with maximum battery output power greater than the load power, so the generators stop; and (b) the battery SOC is between b_{lower} and b_{upper}, the total load power is greater than the output power of generators, but it is less than the sum of maximum battery power and output power of generators. Thus, each generator can either work in the high efficiency region or stop, which is beneficial for fuel saving. The number of the running generators n_G is selected so that the total output power of the generators and the battery can meet the requirement of the total load power.
(3) After every voyage, the battery is charged to an initial amount (SOC_0) via the shore power plant.

4. Multi-objective optimization

4.1. Optimization variables

Considering how the design of the diesel engine, motor, gearbox, and battery affects the performance of plug-in HEPSs, seven design variables are introduced. Among them, five are of component geometry, i.e., the diesel engine displacement V_D, motor rotor diameter d_M, motor rotor length l_M, gear ratio i, and number of the battery modules n_{ser}. Two are constraints related to the energy management strategy, i.e., the SOC lower bound b_{lower} and upper bound b_{upper}. The vector of design variables is expressed as follows.

$$\mathbf{x} = (V_D, D_M, l_M, i, n_{ser}, b_{lower}, b_{upper})^{\mathrm{T}}. \tag{30}$$

4.2. Objective function

In this study, two indexes are used to assess the performance of plug-in HEPSs, namely, the fuel consumption and GHG emissions. They are represented by $f_1(\mathbf{x})$ and $f_2(\mathbf{x})$, respectively. Since it is required to minimize the two indexes simultaneously, the mathematical expression of the objective can be described as below.

$$\min\{f_1(\mathbf{x}), f_2(\mathbf{x})\}. \tag{31}$$

4.2.1. Fuel consumption $f_1(\mathbf{x})$

The annual fuel consumption m_{f_year} of the plug-in HEPS is expressed as:

$$f_1(\mathbf{x}) = m_{f\_year} = \int \dot{m}_f dt. \tag{32}$$

4.2.2. GHG emissions $f_2(\mathbf{x})$

The GHG emissions account for the emissions from consumed diesel fuel and electricity from the shore power supplier. The total annual GHG emissions, denoted by GHG_{year}, is calculated as below.

$$f_2(\mathbf{x}) = GHG_{year} = E_{f\_year} G_{fuel} + E_{e\_year} G_{ele}. \tag{33}$$

$$E_{f\_year} = \frac{m_{f\_year} L_{CV}}{F_{kWh\_J}}. \tag{34}$$

where E_{f_year} and E_{e_year} denote the annually consumed energy from diesel fuel and from the shore power supplier (unit: kWh), respectively; G_{fuel} and G_{ele} are the lifecycle GHG emission coefficients of diesel fuel and shore supplied electricity (unit: kg/kWh), respectively; L_{CV} is the lower calorific value of diesel fuel (unit: J/kg); and F_{kWh_J} is the conversion factor from kWh to J.

In China, 75% of the electricity is produced by thermal power plants, which have an average coal consumption of 0.33 kg/kWh[41]. Therefore, the value of G_{ele} can reach 0.86 kg/kWh[42]. The GHG emissions of the diesel fuel account for two processes, i.e., the Well-to-Tank (WTT) process and the Tank-to-Propeller (TTP) process. During the WTT process, the GHG emissions originate from crude extraction, crude transport, fuel refining, fuel distribution, fuel dispensing, etc. During the TTP process, the GHG derive from the engine combustion. Therefore, the lifecycle GHG emission coefficient G_{fuel} can be calculated by Ref. [13].

$$G_{fuel} = G_{fuel-WTT} F_{kWh\_J} + \frac{G_{fuel\_TTP} F_{kWh\_J}}{L_{CV}}. \tag{35}$$

where G_{fuel_WTT} is the GHG emission coefficient during the WTT process (unit: kg/J), G_{fuel_TTP} is the GHG emission coefficient during the TTP process (dimensionless quantity). By given $G_{fuel\_WTT} = 1.42 \times 10^{-8}$ kg/J, $G_{fuel\_TTP} = 3.17$, $L_{CV} = 4.27 \times 10^7$ J/kg, and $F_{kWh\_J} = 3.60 \times 10^6$, the lifecycle GHG emission coefficient of diesel fuel G_{fuel} can be calculated as 0.32 kg/kWh[43].

4.3. Constraints

The objective functions, defined in the previous section and which should be minimized, are subject to several technical constraints. In the following, the constraints of the surveyed problems are expressed.

4.3.1. Power balance constraint

The power generation and battery dispatch should meet the power demand including propulsive load, hotel load, and service load.

$$n_G P_G + P_B = P_{req}. \tag{36}$$

$$P_{req} = P_{M\_in} + P_{hot} + P_{ser}. \tag{37}$$

where P_{hot} and P_{ser} denote hotel load and service load, respectively.

4.3.2. Generator set constraint

The rated power of the two generator sets should be greater than the maximum required power.

$$2P_{G\_rate} > \sup_t P_{req}. \tag{38}$$

In addition, the time interval of adjacent start/stop operations of each generator set should be greater than a minimum time limitation $t_{\min}$.

$$t_{k+1,i} - t_{k,i} \geq t_{\min};\ \forall i = 1, 2. \tag{39}$$

where $t_{k,i}$ is the time of the i^{th} start/stop operation of the generator set.

4.3.3. Battery constraint

The number of battery modules must be lower than the maximum limit (n_{ser_max}) to make sure the battery can be arranged

in a small cabin.

$$n_{ser} \leq n_{sermax}. \tag{40}$$

The allowed range of *SOC* is determined by considering the stable open-circuit voltage and safety of the batteries [5].

$$10\% \leq SOC \leq 95\%. \tag{41}$$

4.3.4. Ship speed constraint

The required sailing speed v_{req} should be lower than the maximum speed limitation v_{max}.

$$v_{req} \leq v_{max}. \tag{42}$$

4.4. Optimization algorithm

NSGA-II, a kind of fast and elitist algorithm evolved from traditional genetic algorithm (GA), is one of the most efficient and widely used multi-objective evolutionary algorithms. This algorithm employs two procedures named fast non-dominated sorting and density estimation to comprehensively evaluate solutions on multiple objectives [44]. The fast, non-dominated sorting procedure is responsible to sort individuals based on the domination count. The density estimation procedure calculates the average distance between one solution and its nearest neighbor on either side of this point along each objectives [44]. If two individuals have the same domination count, the algorithm prefers the one with lesser crowding distance.

As described in Fig. 4, the algorithm starts with the random generation of initial parent population P_0 of size N, which is used to create initial offspring population Q_0 of size N by the genetic operator of crossover and mutation [45]. Next, P_0 and Q_0 are united as one combined population $R_0 = P_0 \cup Q_0$. Then the algorithm applies fast non-dominated sorting and density estimation to evaluate the multi-objective fitness of every individual in R_0. After that, members of the first several domination count sets are chosen for the new population P_1 successively, until no more sets can be accommodated [44]. The redundant individuals in the last non-dominated set are eliminated through comparison of crowding distance. The new population P_1 is subsequently used to create a new offspring population Q_1, as done earlier. The process is repeatedly performed until the number n of iterations reach the maximum limit n_{end}.

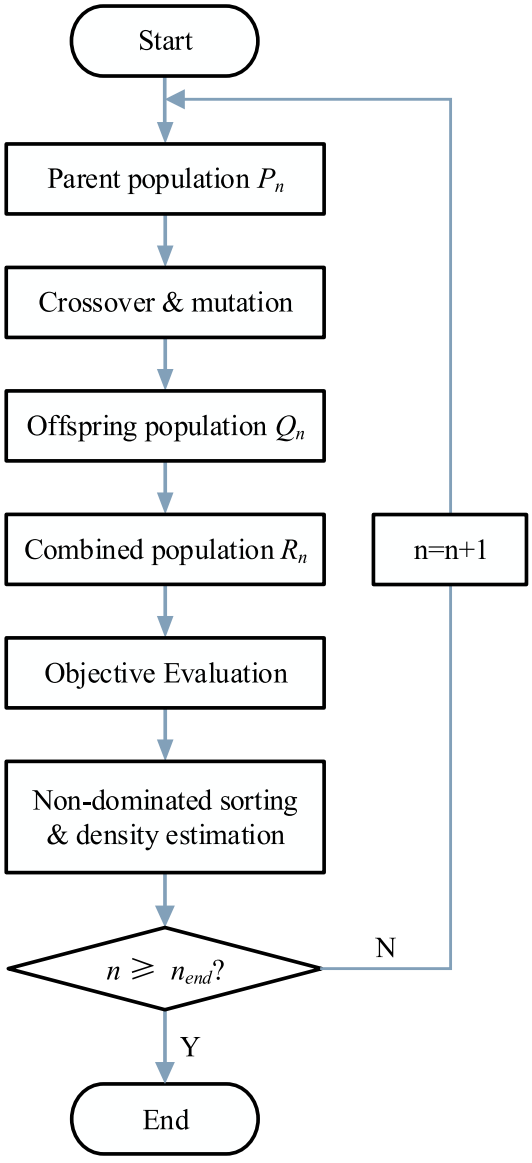

Fig. 4. Flow chart of the optimal process based on NSGA-II.

5. Results and discussion

In this section, the operating cycle of a tug ship is defined considering both propulsive load and non-propulsive load. Following that, the Pareto solution set calculated for the bi-objective optimization is illustrated. Optimal designs can be selected from the solution set. In addition, the results from single-objective optimizations, for minimum fuel consumption and minimum GHG emissions, are provided for comparison.

In order to evaluate the performance of the optimal designs, a real-time hardware-in-the-loop experimental platform was established. Then, performance tests were carried out on the platform. The results from the bi-objective optimization are compared with those from the two single-objective optimizations, and with those from the conventional benchmark vessel.

Furthermore, a sensitivity analysis was conducted to explore the scattered distribution of the design variables and the effects of variations on the solutions of the Pareto front.

5.1. Operating cycle

Due to the absence of a standardized driving cycle, a speed profile of a tug ship based on actual operational data is used in this study [46]. As shown in Fig. 5, the ship sails in two operation modes, namely the transit mode and loading mode. In the transit mode, the AHT sails at a speed above 5.14 m/s (10 kn) to arrive at work sites, and the auxiliary load only contains the hotel load which is about 60 kW as shown in the dark green area in Fig. 5(b). In the loading mode, the AHT is operated at low speed so as to execute lifting or pulling. Therefore, the service load includes the power required by working devices such as a crane, capstan, and bow thrusters. In this study, the operating cycle is run by the proposed AHT 6 times a day and 250 days per year. The battery of plug-in HEPS is recharged from shore power through a ship/shore connecting cable after each operating cycle.

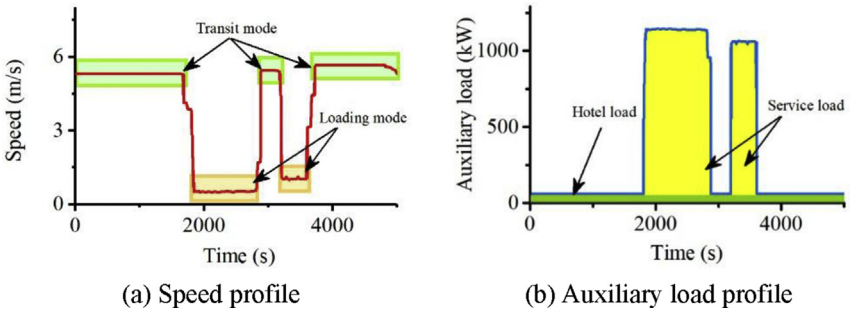

(a) Speed profile (b) Auxiliary load profile

Fig. 5. Speed and auxiliary load profile of the AHT [46].

5.2. Optimization results

The parameters used in the optimization are given in Table A. 1. The ranges of the optimization variables are given in Table A. 2. The Pareto solution set of the proposed bi-objective optimization is illustrated in Fig. 6. Design X and Y are extreme solutions. They gain the minimum fuel consumption and minimum GHG emissions, respectively. The ideal point, located at the intersection point of the minimum fuel consumption and minimum GHG emissions, is impossible to achieve. Therefore, Design M is selected as the optimal design of the present study because it is relative closer to the ideal point. As seen from the fitting curve of the Pareto solutions, the GHG emissions decrease as the fuel consumption increases. In other words, the two performance indices contradict each other. More usage of diesel fuel means less usage of electricity. As mentioned in the subsection on GHG emission modeling, the lifecycle GHG emission coefficient of electricity is two times more than that of diesel fuel. Thus, the reduction of electricity usage can reduce the total GHG emissions considering both the diesel fuel and electricity.

In Fig. 6, Design F is the solution of the single-objective optimization via the classical genetic algorithm aiming to achieve the minimum fuel consumption. It can be observed that the location of Design F almost coincides with that of Design X. Similarly, the location of Design G, which the solution of the single-objective optimization aiming to achieve the minimum GHG emissions, almost coincides with that of Design Y. Other than the optimal designs calculated from the single-objective optimization, the Pareto solution set contains many comprehensive optimal designs regarding both the fuel consumption and GHG emissions.

The optimization variables of Design M, F, and G are compared in Table A. 3. The major difference among the three optimal designs is the number of the battery modules n_{ser}. Design F uses the maximum battery modules (244), which means that the most electricity and the least diesel fuel are consumed. Because the lifecycle GHG emission coefficient of electricity is much higher than that of diesel fuel, the most electricity also means the most GHG emissions. Therefore, Design F gains the minimum fuel consumption, but produces the maximum GHG emissions as shown in Fig. 6. By contrast, Design G uses the minimum battery modules (n_{ser} = 103), with minimum GHG emissions, but has the maximum fuel consumption. The number of battery modules of Design M is between that of Design F and G. Thereafter, Design M achieves the comprehensive optimal performance because its fuel consumption is less than Design G and GHG emissions are less than Design F.

5.3. Discussion

The GHG emissions are dependent on the lifecycle GHG emission coefficient (G_{ele}) of shore supplied electricity. Different generation methods of shore power have different G_{ele}. If the source of the shore power is clean enough, i.e., G_{ele} is small enough, then less fuel consumption of the plug-in HEPS can produce less GHG emissions. In other word, the contradiction between fuel consumption and GHG emissions can be resolved. In this regard, there exists an optimal solution which can reach minimum fuel consumption and minimum GHG emissions simultaneously.

In order to verify the dependence of the optimization objectives on G_{ele}, the optimization results from G_{ele} = 0.86kg/kWh, considering the shore power comes from coal, are compared with the results from other two smaller values of G_{ele}. As shown in Fig. 7, the

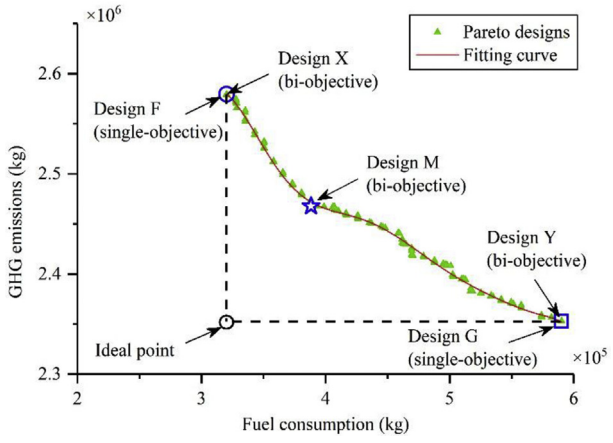

Fig. 6. Comparison of optimization results.

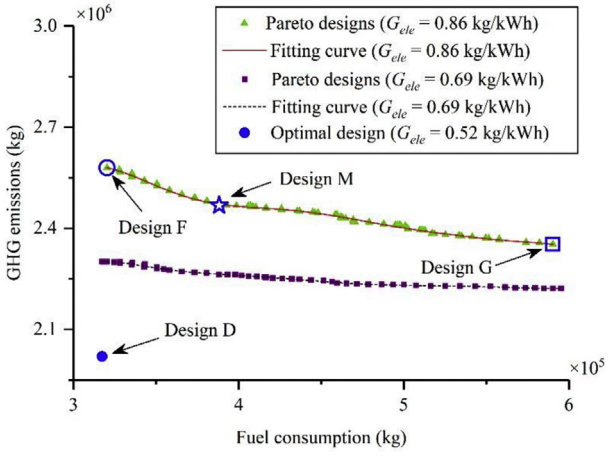

Fig. 7. Optimization results from different GHG emission coefficients.

Pareto solutions for $G_{ele} = 0.69$kg/kWh evidently lead to lower GHG emissions compared with those for $G_{ele} = 0.86$kg/kWh. The slopes of the fitting curves of the two Pareto solution sets are both negative, which indicates the contradiction between fuel consumption and GHG emissions. However, the slope of the fitting curve of $G_{ele} = 0.69$kg/kWh is much flatter than that of $G_{ele} = 0.86$kg/kWh. Therefore, less GHG emissions are produced for $G_{ele} = 0.69$kg/kWhwhen less fuel is consumed.

When $G_{ele} = 0.52$kg/kWh, the optimal solutions converge to Design D. That is to say, no other solution can be superior to Design D in either fuel consumption or GHG emissions. The optimization variables of Design D are given in Table A. 3. Compared with Design M, Design D has smaller engine and wider range of SOC. Therefore, Design D is allowed to use more electricity from the shore power and consume less fossil fuel. The GHG emissions from the increased electricity are low because of the small G_{ele}. Consequently, Design D can provide the minimum fuel consumption and minimum GHG emissions. These results are in accordance with the aforementioned hypothesis, which verifies the accuracy of the models and algorithm in this study.

5.4. Hardware-in-the-loop experiment

A hardware-in-the-loop (HIL) experiment is performed to verify the results of the optimization. The HIL experimental platform, as shown in Fig. 8, is established including a real-time plug-in HEPS model platform and a real-time energy management platform. The software and hardware of the HIL platform can be developed via MATLAB toolboxes for online calibration and C language rapid generation.

The development process of the HIL experiment platform consists of three steps. Firstly, the driveline models and energy management strategy are built in the MATLAB environment. Secondly, the real-time kernel of the driveline models is generated by MATLAB/Simulink automatic code generation technology, as well as the real-time kernel of the energy management strategy. Thirdly, the dSPACE software tool, named ControlDesk, downloads the real-time kernel of the driveline models into the dSPACE hardware PX10 which has strong real-time computing capacity. In addition, the kernel of the energy management strategy is downloaded into the MicroAutobox which is an electronic control hardware. The variables in the PX10 and the MicroAutobox can be monitored and calibrated through ControlDesk running on a desktop.

The CAN and I/O interfaces are used for the communication between the PX10 and the MicroAutobox. The communication with the ControlDesk is through a ethernet interface.

The driveline of a conventional tug ship is taken as the benchmark for the studied plug-in HEPS. The parameters of the tug ship are listed in Table A. 4. The output power of the generator sets is controlled by a proportional-integral-derivative (PID) controller that tracks the power command [5]. In order to reduce fuel consumption, the second generator set does not work until the previous generator set cannot provide sufficient load power. The results from the conventional propulsive system are represented by "Conv." in Figs. 9 and 10. Regarding the optimal design of the plug-in HEPS, in addition to the Design M selected from the Pareto

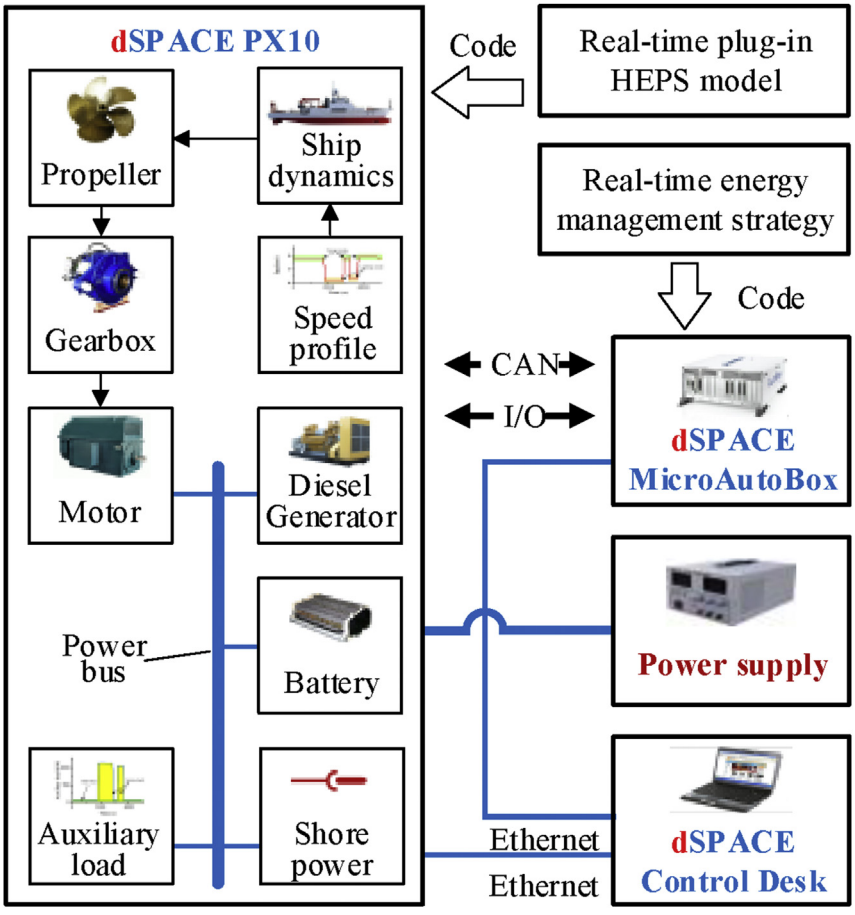

Fig. 8. Schematic diagram of the HIL experimental platform.

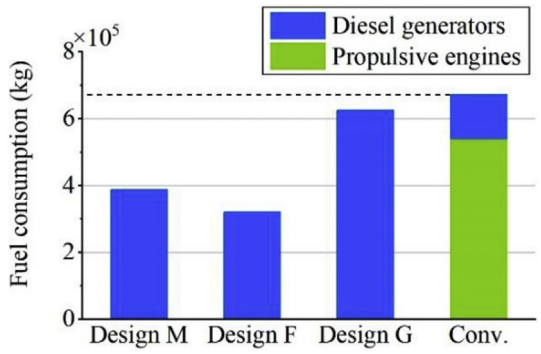

Fig. 9. Annual fuel consumption.

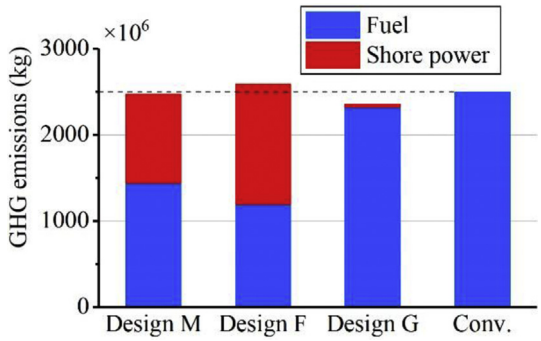

Fig. 10. Annual GHG emissions.

solution set of the proposed bi-objective optimization, Design F and G, which respectively pursue fuel consumption and GHG emissions by the single-objective optimization, were also implemented for comparison. The performance of Design M, F, G, and the conventional propulsive system are compared in terms of fuel consumption and GHG emissions.

As shown in Fig. 9, the fuel consumption of Design M, F, G, and the conventional propulsion system is 3.88×10^5 kg, 3.20×10^5 kg, 6.25×10^5 kg, and 6.72×10^5 kg, respectively. Hence, all of the three plug-in HEPSs achieve less fuel consumption than the conventional propulsion system. Specifically, Design M, F, and G can reduce fuel consumption by 42.26%, 52.38%, and 6.99%, respectively. When compared with Design F, which aimed at minimum fuel consumption, Design M increases fuel consumption by 20.6%. When compared with Design G, which aimed at minimum GHG emissions, Design M decreases fuel consumption by 37.9%.

As shown in Fig. 10, GHG emissions from Design M, F, G, and the conventional propulsion system are 2.47×10^6 kg, 2.59×10^6 kg, 2.35×10^6kg, and 2.49×10^6 kg, respectively. Compared with the conventional propulsion system, Design M and G reduce the GHG emissions by 0.91% and 5.64%, respectively, while Design F increases GHG emissions by 3.71%. When compared with Design F, Design M decreases GHG emissions by 4.6%. When compared with Design G, which aimed at minimum GHG emissions, Design M increases GHG emissions by 5.1%.

Overall, Design M is better than Design F in terms of GHG emissions, and it is better than Design G (only pursing minimum GHG emissions) in terms of fuel consumption. Therefore, Design M is closer to the ideal point than Design F and G as shown in Fig. 6.

According to the energy management strategy, one or two diesel generators can either be shut down or work with high efficiency at most of the working time, owing to the usage of large capacity batteries. Therefore, fuel consumption can be reduced by using fewer diesel engines. The working schedules of the diesel engines are provided in Fig. 11 for the four designs. One or two diesel engines of the plug-in HEPS can stop working or consume no fuel for some time during the operating cycle. In contrast, at least one diesel engine of the conventional propulsion system stays working all the time. Further, the accumulated working time per day of the diesel engines in Design M, F, and G is 13680s, 10800s, and 22320s, respectively, compared to 39240s in the conventional propulsion system. It can be observed that the working time of the diesel engines correspond to the fuel consumption as shown in Fig. 9.

Although large amounts of electricity allow significant fuel saving, GHG emissions may increase due to the large GHG intensity of the electricity from the shore power plant. Design F is the extreme example. As seen from Fig. 12, Design F consumes the maximum electricity (1.69×10^6 kWh) from the shore power plant. Accordingly, Design F produces the maximum GHGs as seen in Fig. 10, despite the minimum fuel consumption as seen in Fig. 9. Compared with Design F, Design M consumes less electricity (1.24×10^6 kWh), therefore, produces less GHG emissions. Nevertheless, it consumes more diesel fuel. As a whole, Design M is a trade-off optimal solution with relatively lower fuel consumption and GHG emissions.

5.5. Sensitivity analysis

First, the scattered distribution of the seven optimization variables along with the population in the Pareto frontier are provided in Fig. 13 in order to determine the most sensible variables which are useful for further study. Three of the seven variables, i.e., motor rotor diameter d_M, motor rotor length l_M, and gear ratio i, remain almost unchanged as shown in Fig. 13(b), (c), and (d). This indicates that the three variables do not significantly lead to contradiction between the two objective indices. Among the other four, the diesel engine displacement V_D, shown in Fig. 13(a), is special because it is always close to one of the two values, i.e., 70×10^{-3}m^3 and 81×10^{-3}m^3. In contrast, the remaining variables, i.e., number of battery modules n_{ser}, lower bound of SOC b_{lower}, and upper bound of SOC b_{upper}, are scattered within the allowable range as shown in Fig. 13(e–g). Thus, these three variables do not converge regarding the two performance indices. This indicates that the variable either leads to significant contradiction between the two indices or has no influence on them. The details are revealed in the following paragraphs by calculating the effects of the variable variations.

Second, the effects of variations of the seven optimization variables on the performance of the Pareto solutions are investigated. In addition to validate the proposed bi-objective optimization, for a meaningful investigation, it is important to predict the performance even if the optimal design cannot be accurately realized due to complex engineering issues such as materials and manufacturing obstacles. Three designs are selected from the Pareto front, Design M, X, and Y (see Fig. 6). Each optimization variable ranges from small to large values within the allowable range defined in Table A. 2. The performance is evaluated regarding the two indices, fuel consumption and GHG emissions, as shown in Fig. 13, in which the arrows indicate the performance change trend as the optimization variable changes from small to large.

The variation of the diesel engine displacement V_D affects the performance of Design M, X, and Y in different ways, as seen in Fig. 14(a). No point other than Design M, X, and Y can achieve better performance regarding the two indices. These results validate the accuracy of the bi-objective optimization proposed in this study. Specifically, as V_D decreases, Design M and X present lower fuel consumption with almost unchanged GHG emissions. Design Y also

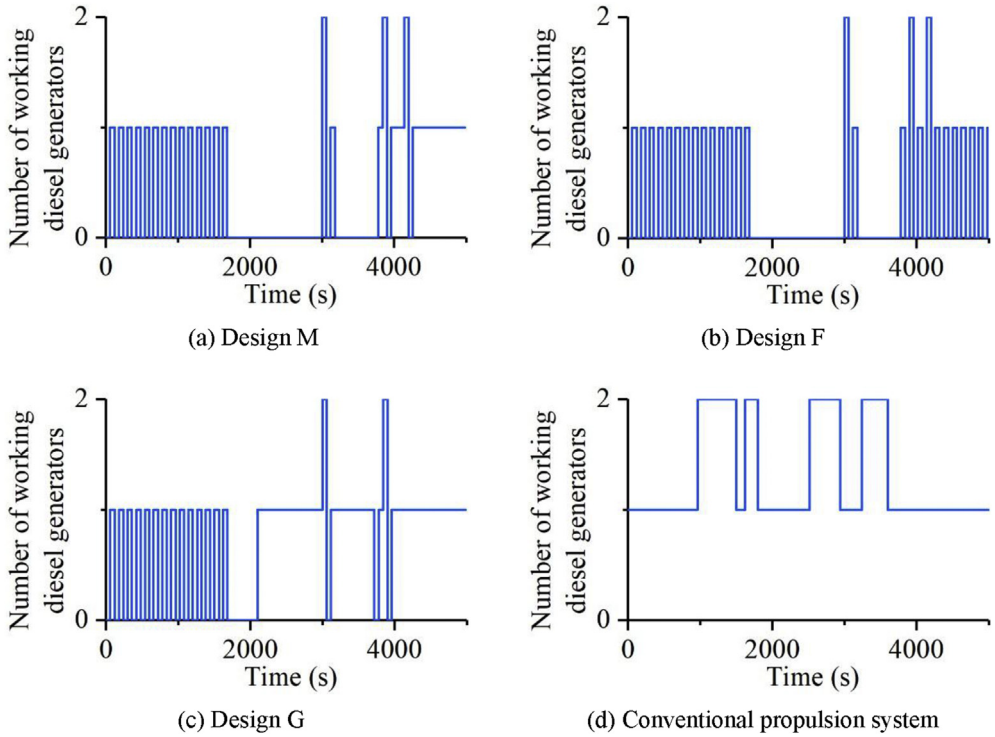

Fig. 11. Working schedule of the generator sets.

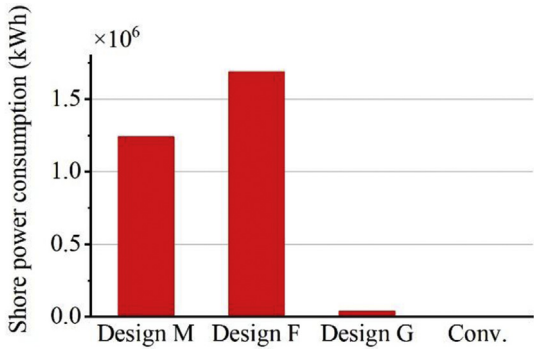

Fig. 12. Annual shore power consumption.

presents lower fuel consumption but higher GHG emissions. As V_D increases, Design M leads to higher fuel consumption with slightly higher GHG emissions. However, Design X presents higher fuel consumption with almost unchanged GHG emissions, and Design Y leads to lower fuel consumption but higher GHG emissions.

The effects of variations on motor rotor diameter d_M are illustrated in Fig. 14(b). The change trends of Design M, X, and Y are similar. As d_M decreases, the three optimal designs lead to higher fuel consumption and GHG emissions. As d_M increases, they present a significantly higher fuel consumption and GHG emissions. Therefore, Design M, X, and Y are actually local optimal in their neighborhoods. A similar trend regarding variations on motor rotor length l_M and gear ratio i can be observed in Fig. 14(c) and (d).

The effects of variations on the number of battery modules n_{ser} are illustrated in Fig. 14(e). The change trends of Design M, X, and Y are similar. As n_{ser} increases, the three optimal designs lead to lower fuel consumption but higher GHG emissions. As n_{ser} decreases, they present higher fuel consumption but lower GHG emissions. Therefore, no point can be dominant over the others. Intuitively, this change trend is in line with the Pareto front. The comparison between the variation designs and the Pareto front around Design M is plotted in the zoom-in figure at the top right corner of Fig. 14(e). Their change trend is the same, but there are solutions in the Pareto front which are better than the variation designs, regarding both performance indices. The explanation for the change trend is that more battery modules allows more electricity usage, and consequently, less fuel consumption. Consequently, GHG emissions become higher because the lifecycle GHG emission coefficient of electricity produced by coal is two times more than that of diesel fuel.

The effects of variations on the lower bound of the battery SOC b_{lower} are illustrated in Fig. 14(f). The change trends of Design M, X, and Y are contrary to those of the number of battery modules in Fig. 14(e). As b_{lower} increases, the three optimal designs present higher fuel consumption but lower GHG emissions. As b_{lower} gets smaller, they lead to lower fuel consumption but higher GHG emissions. Therefore, no point can be dominant over the others. The comparison between the variation designs and the Pareto front around Design M is plotted in the zoom-in figure at the top right corner of Fig. 14(f). Their change trend is the same, but there are solutions in the Pareto front which are better than the variation designs regarding both performance indices. The explanation for the change trend is that lower b_{lower} allows higher electricity usage, and consequently, lower fuel consumption and higher GHG emissions. On the other hand, variations on the upper bound of battery SOC b_{upper} present no observable effect on the performance of the three optimal designs as shown in Fig. 14(g). The upper bound b_{upper} of Design M, X, and Y are 82.92%, 83.34%, and 80.03%, respectively. Thus, the difference between them is not significant. Overall, the battery SOC barely reaches the boundary during the voyage due to the large battery capacity provided by increased use of battery modules. Therefore, the performance is not sensitive to variations on the upper bound b_{upper}.

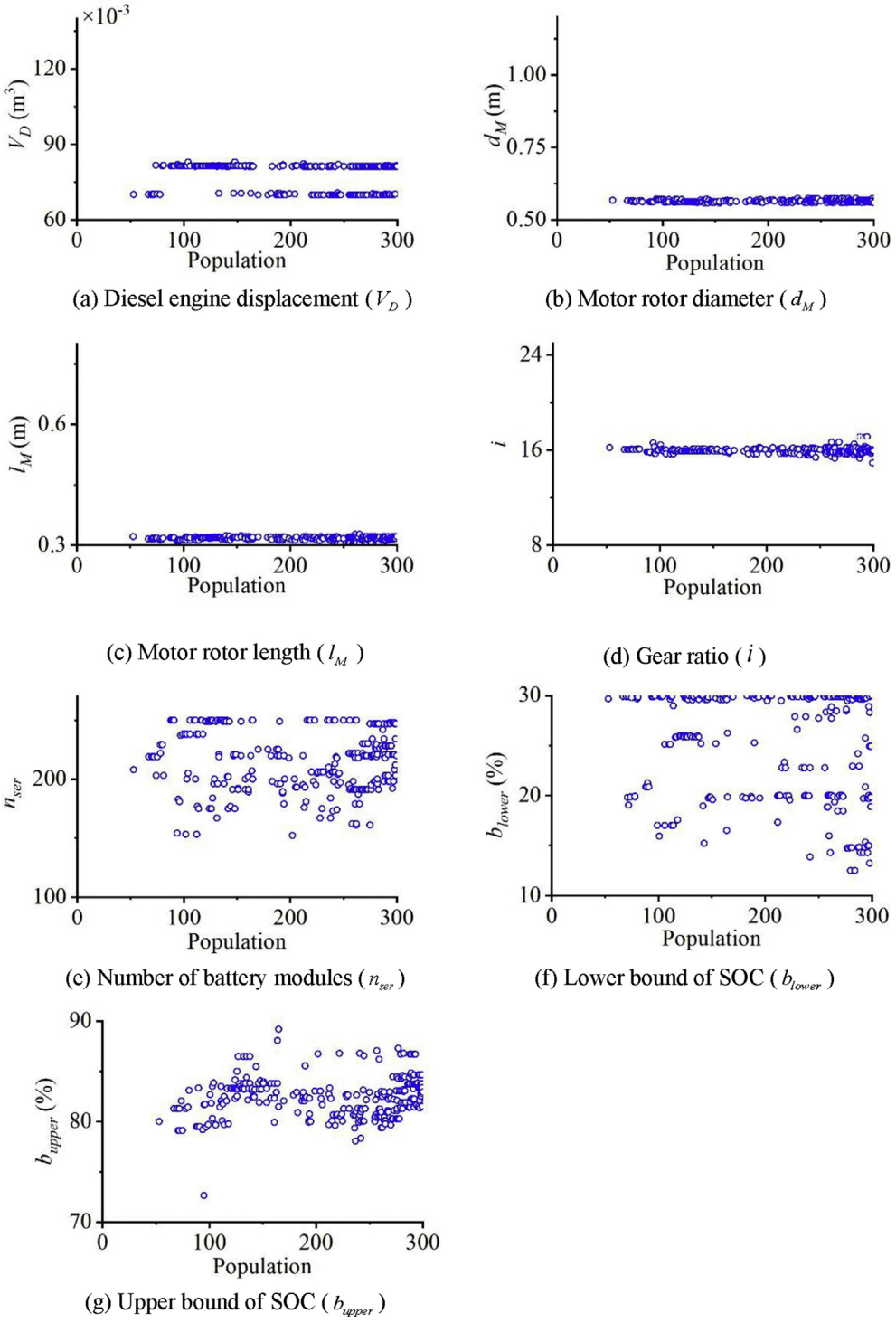

Fig. 13. Scattered distribution of optimization variables with population in Pareto front.

6. Conclusion

A bi-objective optimization was proposed for the design of a plug-in HEPS, considering not only fuel consumption but also GHG emissions. The NSGA-II method was used to explore the Pareto optimal solution set. A real-time HIL experimental platform was built to validate the effectiveness of the optimization. The experimental results showed that the optimal design selected from the Pareto solution set of the bi-objective optimization can achieve 37.9% lower fuel consumption than the single-objective optimization which pursues only GHG emissions. At the same time, 4.6% less GHG are emitted in comparison with the single-objective optimization which pursues only fuel consumption. Moreover, compared with the conventional propulsion system, the NSGA-II has advantages in both aspects, i.e., 42.26% lower fuel consumption and 0.91% lower GHG emissions. Further, according to a sensitivity analysis regarding variations of the seven optimization variables, three variables (motor rotor diameter, motor rotor length, and gear ratio)

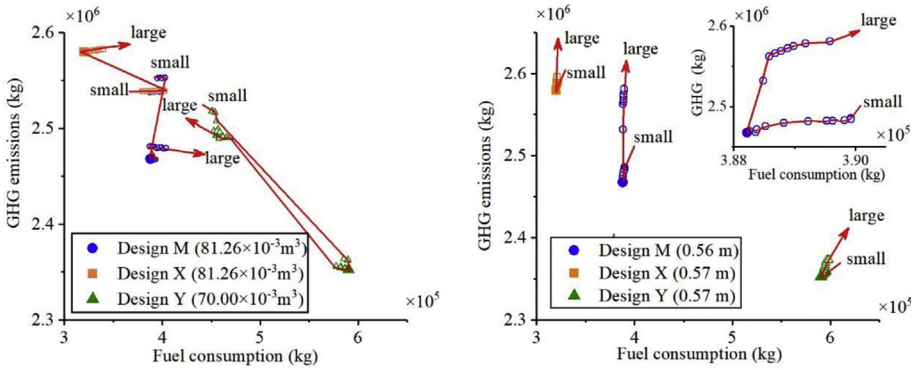

(a) Effects of diesel engine displacement (V_D)

(b) Effects of motor rotor diameter (d_M)

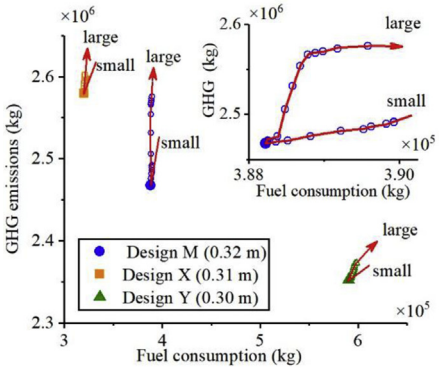

(c) Effects of motor rotor length (l_M)

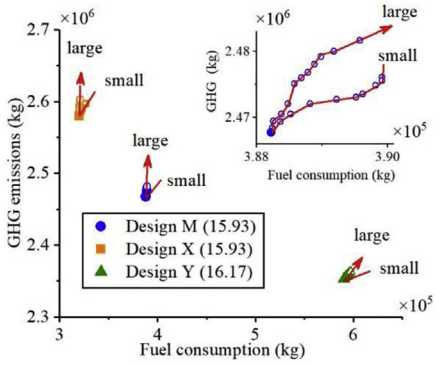

(d) Effects of gear ratio (i)

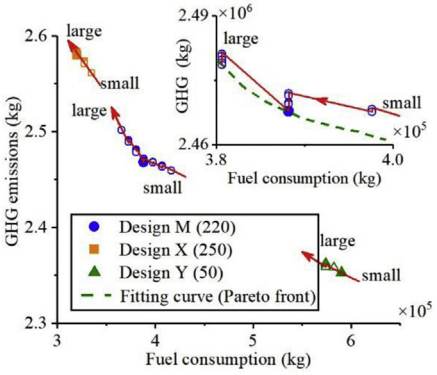

(e) Effects of number of the battery modules

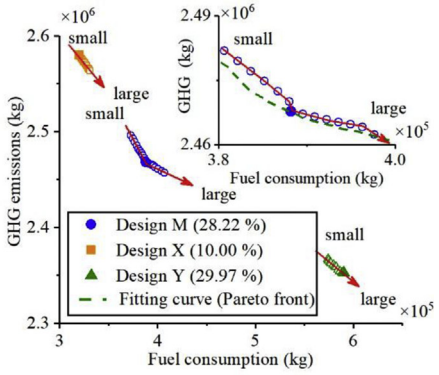

(f) Effects of SOC lower bound (b_{lower})

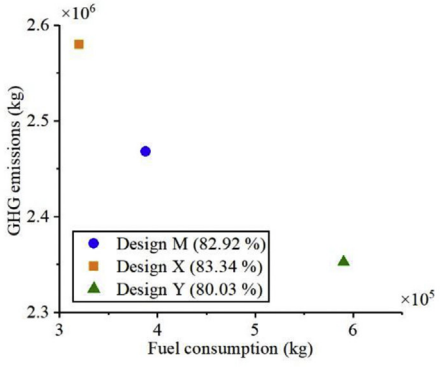

(g) Effects of SOC upper bound (b_{upper})

Fig. 14. Effects of variations of the seven optimization variables.

are of local optimum at the Pareto front; and two (number of battery modules and lower bound of the battery SOC) are of strong sensitivity regarding the contradiction between fuel consumption and GHG emissions. This study is of great significance in areas where electricity is mainly produced from coal and GHG emission reduction is difficult because the lifecycle GHG emission coefficient of the shore supplied electricity is more than two times that of the diesel fuel. The proposed bi-objective method can be applied to the design of various HEPSs, such as offshore vessels, research, and exploration vessels.

Acknowledgement

The present research was financially supported by the National Natural Science Foundation of China (No. 51475284).

Appendix

Table A. 1
Values of parameters used in the simulation [4,11,26,28,43,47–49].

Parameter	Nomenclature	Value
A_e/A_o	expanded blade–area ratio	0.5445
A_T	advance facing area in the air	128.60 m^2
C_{Air}	air resistance coefficient	0.8
C_F	frictional resistance coefficient	2.2700×10^{-3}
C_W	wave-making resistance coefficient	2.7500×10^{-3}
F_{kWh_J}	conversion factor from kWh to J	3.60×10^6
G_{fuel_TTP}	GHG emission coefficient during the TTP process	3.17
G_{fuel_WTT}	GHG emission coefficient during the WTT process	1.42×10^{-8} kg/J
G_{ele}	lifecycle GHG emission coefficient of shore supplied electricity	0.86 kg/kWh
L_{CV}	lower calorific value of diesel fuel	4.27×10^7 J/kg
Q_{bat}	battery capacity	41 Ah
S	wet-surface area of hull	1347.12 m^2
SOC_0	initial state of charge of the battery	90%
Z	number of the propeller blades	4
m	ship mass	1.7000×10^6 kg
n_{end}	maximum number of iterations	300
n_p	number of the propellers	2
n_{ser_max}	maximum number of the battery modules	250
$pitch/D$	pitch ratio	0.702
t_1	thrust deduction coefficient	0.1000
t_{min}	minimum duration of the generator start/stop operation	60 s
v_{req}	maximum speed limitation	7.72 m/s (15 kn)
η_{gear}	efficiency coefficient of the gearbox	0.98
η_{gen}	efficiency coefficient of the generator	0.97
ρ	sea-water density	1.025×10^3 kg/m^3
υ	kinematic viscosity of sea water	1.1883×10^6 m^2s^{-1}

Table A. 2
Range of the optimization variables

Optimization variable	Lower bound	Upper bound
displacement of the diesel engine $V_D(10^{-3}\ m^3)$	70	140
diameter of the motor rotor $d_M(m)$	0.30	0.75
length of the motor rotor $l_M(m)$	0.25	0.95
gear ratio i	8.00	20.00
number of the battery modules n_{ser}	50	250
SOC lower bound $b_{lower}(\%)$	10	30
SOC upper bound $b_{upper}(\%)$	70	90

Table A. 3
Comparison among the four optimal designs.

Optimization variable	Design M	Design F	Design G	Design D
$V_D(10^{-3}m^3)$	81.26	81.26	83.16	80.50
$d_M(m)$	0.56	0.51	0.67	0.57
$l_M(m)$	0.32	0.54	0.30	0.32
i	15.93	17.94	16.12	9.21
n_{ser}	220	244	103	244
$b_{lower}(\%)$	28.22	13.56	29.81	13.32
$b_{upper}(\%)$	82.92	87.74	88.52	86.55

Table A. 4
Specification of a 120 ton bollard pull AHT [50].

Parameter	Value
Length (oa)	66.00 m
Length (pp)	57.00 m
Breadth	16.00 m
Depth	7.30 m
Draught	6.20 m
Rated power of the propulsive engines	2 × 3285 kW
Rated power of the generators	2 × 720 kW
Gear ratio	800:141

References

[1] Zhu Y, Zhou S, Feng Y, Hu Z, Yuan L. Influences of solar energy on the energy efficiency design index for new building ships. Int J Hydrogen Energy 2017;42:19389–94.
[2] Mccarthy JH. On the calculation of thrust and torque fluctuations of propellers in nonuniform wake flow. Sensor Actuator B Chem 1961;161(1):80–7.
[3] Díaz-De-Baldasano MC, Mateos FJ, Núñez-Rivas LR, Leo TJ. Conceptual design of offshore platform supply vessel based on hybrid diesel generator-fuel cell power plant. Appl Energy 2014;116(3):91–100.
[4] Baldi F, Ahlgren F, Melino F, Gabrielii C, Andersson K. Optimal load allocation of complex ship power plants. Energy Convers Manag 2016;124:344–56.
[5] Ovrum E, Bergh TF. Modelling lithium-ion battery hybrid ship crane operation. Appl Energy 2015;152:162–72.
[6] Guidi G, Suul JA, Jenset F, Sorfonn I. Wireless charging for ships: high-power inductive charging for battery electric and plug-in hybrid vessels. IEEE Electrification Magazine 2017;5(3):22–32.
[7] Takamasa T, Oode T, Kifune H, Shimizu E. Quick charging plug-in electric boat "RAICHO-I". In: IEEE electric ship technologies symposium, alexandria, USA; 2011.
[8] Zhou G, Ou X, Zhang X. Development of electric vehicles use in China: a study from the perspective of life-cycle energy consumption and greenhouse gas emissions. Energy Policy 2013;59(3):875–84.
[9] Shin J, Lee JH, Realff MJ. Operational planning and optimal sizing of microgrid considering multi-scale wind uncertainty. Appl Energy 2017;195:617–33.
[10] Soleymani M, Yoosofi A, Kandi -DM. Sizing and energy management of a medium hybrid electric boat. J Mar Sci Technol 2015;20(4):739–51.
[11] Skinner BA, Parks GT, Palmer PR. Comparison of submarine drive topologies using multiobjective genetic algorithms. IEEE Veh Technol 2009;58(1):57–68.
[12] Sciberras EA, Norman RA. Multi-objective design of a hybrid propulsion system for marine vessels. IET Electr Syst Transp 2012;2(3):148–57.
[13] Ribau JP, Silva CM, Sousa JMC. Efficiency, cost and life cycle CO2 optimization of fuel cell hybrid and plug-in hybrid urban buses. Appl Energy 2014;129(129):320–35.
[14] Fang L, Qin S, Xu G, Li T, Zhu K. Simultaneous optimization for hybrid electric vehicle parameters based on multi-objective genetic algorithms. Energies 2011;4(3):532–44.
[15] Völker T. Hybrid propulsion concepts on ships. In: 33rd international scientific conference "science in practice"; 2015. p. 66–76. Schweinfurt, Germany.
[16] Mokryani G. Active distribution networks planning with integration of demand response. Sol Energy 2015;122(3):1362–70.
[17] Mora AM, Merelo JJ, Castillo PA, Arenas MG. HCHAC: a family of MOACO algorithms for the resolution of the bi-criteria military unit pathfinding problem. Comput Oper Res 2013;40(6):1524–51.
[18] Ahmadi MH, Ahmadi MA, Mehrpooya M, Sameti M. Thermo-ecological analysis and optimization performance of an irreversible three-heat-source absorption heat pump. Energy Convers Manag 2015;90:175–83.
[19] Ahmadi MH, Ahmadi MA, Bayat R, Ashouri M, Feidt M. Thermo-economic optimization of Stirling heat pump by using non-dominated sorting genetic algorithm. Energy Convers Manag 2015;91:315–22.
[20] Ahmadi MH, Ahmadi MA, Sadatsakkak SAJR, Reviews SE. Thermodynamic analysis and performance optimization of irreversible Carnot refrigerator by using multi-objective evolutionary algorithms (MOEAs). Renew Sustain

Energy Rev 2015;51:1055–70.
[21] Sadatsakkak SA, Ahmadi MH, Ahmadi M. Thermodynamic and thermo-economic analysis and optimization of an irreversible regenerative closed Brayton cycle. Energy Convers Manag 2015;94:124–9.
[22] Sánchez-Orgaz S, Pedemonte M, Ezzatti P, Curto-Risso PL, Medina A, Hernández AC. Multi-objective optimization of a multi-step solar-driven Brayton plant. Energy Convers Manag 2015;99. 346-58.
[23] Ghodratnama A, Jolai F, Tavakkoli-Moghaddam R. Solving a new multi-objective multi-route flexible flow line problem by multi-objective particle swarm optimization and NSGA-II. J Manuf Syst 2015;36:189–202.
[24] Possel B, Wismans LJJ, Berkum ECV, Bliemer MCJ. The multi-objective network design problem using minimizing externalities as objectives: comparison of a genetic algorithm and simulated annealing framework. Transportation 2017: 1–28.
[25] Fröberg A. Extending the inverse vehicle propulsion simulation concept-to improve simulation performance. In: Thesis no. 1181, linköping studies in science and technology. Sweden: Linköpings Universitet; 2005.
[26] Holtrop J, Mennen GGJ. An Approximate power prediction method. Int Shipbuild Prog 1982;29(335):166–70.
[27] Carlton JS. Marine propellers and propulsion. third ed. Oxford, U.K.: Butter-worth-Heinemann; 2012.
[28] Hou J, Sun J, Hofmann HF. Mitigating power fluctuations in electric ship propulsion with hybrid energy storage system: design and analysis. IEEE J Ocean Eng 2017;99:1–15.
[29] Bernitsas MM. KT, KQ and efficiency curves for the Wageningen B-series propellers. Technical Report. University of Michigan; 1981.
[30] Rizzoni G, Guzzella L, Baumann BM. Unified modeling of hybrid electric vehicle drivetrains. IEEE ASME Trans Mechatron 1999;4(3):246–57.
[31] Pisu P, Rizzoni G. A comparative study of supervisory control strategies for hybrid electric vehicles. IEEE Trans Control Syst Technol 2007;15(3):506–18.
[32] Sundstrom O, Guzzella L, Soltic P. Torque-assist hybrid electric powertrain sizing: from optimal control towards a sizing law. IEEE Trans Control Syst Technol 2010;18(4):837–49.
[33] Sorrentino M, Mauramati F, Arsie I, Cricchio A, Pianese C, Nesci W. Application of Willans line method for internal combustion engines scalability towards the design and optimization of eco-innovation solutions. 2015. p. 468–76. SAE Technical Paper 2015-24-2397.
[34] Divya KC, Østergaard J. Battery energy storage technology for power systems—an overview. Electr Power Syst Res 2009;79(4):511–20.
[35] Xu L, Mueller CD, Li J, Ouyang M, Hu Z. Multi-objective component sizing based on optimal energy management strategy of fuel cell electric vehicles. Appl Energy 2015;157:664–74.
[36] Chen BC, Wu YY, Tsai HC. Design and analysis of power management strategy for range extended electric vehicle using dynamic programming. Appl Energy 2014;113(1):1764–74.
[37] Onori S, Serrao L, Rizzoni G. Hybrid electric vehicles. London: Springer; 2016.
[38] Johnson VH. Battery performance models in ADVISOR. J Power Sources 2002;110(2):321–9.
[39] Zahedi B, Norum LE, Ludvigsen KB. Optimized efficiency of all-electric ships by dc hybrid power systems. J Power Sources 2014;255(-):341–54.
[40] Hung YH, Tung YM, Chang CH. Optimal control of integrated energy management/mode switch timing in a three-power-source hybrid powertrain. Appl Energy 2016;173:184–96.
[41] Yang Y, Yang Z, Xu G, Wang N. Situation and prospect of energy consumption for China's thermal power generation. Proc CSEE 2013;(23):1–11.
[42] Wang B, Min X, Li Y. Study on the economic and environmental benefits of different EV powertrain topologies. Energy Convers Manag 2014;86(86): 916–26.
[43] Edwards R, Mahieu V, Griesemann J-C, Larivé J-F, Rickeard DJ. Well-to-wheels analysis of future automotive fuels and powertrains in the European context. SAE Trans 2004:1072–84.
[44] Deb K, Pratap A, Agarwal S, Meyarivan T. A fast and elitist multiobjective genetic algorithm: NSGA-II. IEEE Trans Evol Comput 2002;6(2):182–97.
[45] Rabiee M, Zandieh M, Ramezani P. Bi-objective partial flexible job shop scheduling problem: NSGA-II, NRGA, MOGA and PAES approaches. Int J Prod Res 2012;50(24):7327–42.
[46] Sciberras EA, Zahawi B, Atkinson DJ, Juandó A. Electric auxiliary propulsion for improved fuel efficiency and reduced emissions. Proc Inst Mech Eng J Mater Eng 2015;229(1):36–44.
[47] Sandmo T. The Norwegian Emission Inventory 2011: documentation of methodologies for estimating emissions og greenhouse gases and long-range transboundary air pollutants. Statistics Norway; 2011.
[48] Tsolakis A, Megaritis A, Wyszynski ML, Theinnoi K. Engine performance and emissions of a diesel engine operating on diesel-RME (rapeseed methyl ester) blends with EGR (exhaust gas recirculation). Energy 2007;32(11):2072–80.
[49] Diesel-electric Propulsion Plants: a brief guideline how to engineer a diesel-electric propulsion system. http://marine.man.eu/. Man Diesel, (accessed 15 September 2016).
[50] AHTS propulsion for swire pacific offshore. http://marine.man.eu/, (accessed 30 November 2015).